CetZ tubulin-like proteins control archaeal cell shape

Iain G. Duggin[1,2], Christopher H. S. Aylett[1], James C. Walsh[2,3], Katharine A. Michie[1], Qing Wang[1], Lynne Turnbull[2], Emma M. Dawson[2], Elizabeth J. Harry[2], Cynthia B. Whitchurch[2], Linda A. Amos[1] & Jan Löwe[1]

1. Medical Research Council Laboratory of Molecular Biology, Francis Crick Avenue, Cambridge, CB2 0QH, UK.
2. The ithree institute, University of Technology Sydney, NSW, 2007, Australia.
3. School of Physics, University of New South Wales, Sydney, NSW, 2052, Australia.

Tubulin is a major component of the eukaryotic cytoskeleton, controlling cell shape, structure and dynamics, whereas its bacterial homolog FtsZ establishes the cytokinetic ring that constricts during cell division[1,2]. How such different roles of tubulin and FtsZ evolved is unknown. Archaea may hold clues as these organisms share characteristics with Eukarya and Bacteria[3]. Here we report the structure and function of proteins from a distinct family related to tubulin and FtsZ, named CetZ, which co-exists with FtsZ in many archaea. CetZ crystal structures showed the FtsZ/tubulin superfamily fold, and one crystal form contained sheets of protofilaments, suggesting a structural role. However, inactivation of the CetZs in *Haloferax volcanii* did not affect cell division. Instead, CetZ1 was required for differentiation of the irregular plate-shaped cells into a rod-shaped cell type that was essential for normal swimming motility. CetZ1 formed dynamic cytoskeletal structures *in vivo*, relating to its capacity to remodel the cell envelope and direct rod formation. CetZ2 was also implicated in *H. volcanii* cell shape control. Our findings expand the known roles of the FtsZ/tubulin superfamily to include archaeal cell shape dynamics, suggesting that a cytoskeletal role might predate eukaryotic cell evolution, and they support the premise that a major function of microbial rod-shape is to facilitate swimming.

Many archaea have FtsZ that appears to function in cell division[4-8]. However, unlike bacteria, archaeal genomes frequently contain additional genes belonging to the FtsZ/tubulin superfamily[9]. These genes are abundant in the haloarchaea, which dominate hyper-saline lakes globally[10] and are generally noted for their unusual flattened cell morphologies. Examples include rectangular prisms[11,12], triangles[13], and pleomorphic cells seen in the model organism *H. volcanii*[14]. The molecular basis of cell shape in haloarchaea is unknown.

The largest group of archaeal FtsZs/tubulins clearly distinguishable from the FtsZ and tubulin families is a deeply-rooted family from the phylum Euryarchaeota that we named CetZ (formerly annotated "FtsZ3"[9], or "FtsZ type 2"[15]), after the prototypical member described here: "Cell-structure-related Euryarchaeota tubulin/FtsZ homolog 1" (CetZ1, Fig. 1a). Multiple sequence alignments showed that CetZ family members contain a mosaic of tubulin-like and FtsZ-like amino-acid residues; several of the most conserved residues involved in GTP binding and hydrolysis are identical in CetZ and tubulin (Fig. 1b, blue shading). In some other regions there is stronger sequence similarity between CetZs and FtsZs, leading to a closer apparent relationship of these two families[9,16] (Fig. 1a).

To further investigate these relationships, we solved crystal structures of *H. volcanii* CetZ1 (HVO_2204) and CetZ2 (HVO_0745), from separate orthologous groups, and a divergent CetZ from *Methanosaeta thermophila* (Extended Data Table 1). The structures showed the FtsZ/tubulin core fold, with a C-terminal helical extension (H11) like tubulin, but without the N-terminal helical extension seen in FtsZs (Fig 1c). CetZ2 crystallised as a protofilament with GTPγS that showed subunit interaction geometry, spacing (43 Å subunit repeat) and surface area (941 $Å^2$) consistent with archetypal tubulin and FtsZ protofilaments (Fig 1d). Furthermore, the protofilaments were arranged as 2D sheets, showing lateral interactions between protofilaments consistent with those of FtsZ and tubulin (Extended Data Fig. 1). These CetZ structures suggest a possible cytoskeletal or cytomotive[1] function.

To search for functions of the CetZs, we individually deleted the six *cetZ* open reading frames identified in the *H. volcanii* genome (*e.g. ΔcetZ1*, Fig. 2a and Extended Data Table 2). No differences in growth rate or cell size were detected in the six *ΔcetZ* strains compared to the parent strain (H98), indicating that CetZs are not individually required for cell division (Fig. 2b). To investigate possible functional redundancy amongst the multiple CetZs, we designed a dominant-inhibitory point mutation in CetZ1, the most conserved of the *H. volcanii* CetZs (close orthologs of CetZ1 were found throughout the class Halobacteria; Extended Data Fig. 2). This mutation (CetZ1.E218A, Fig. 1b) was based on well-characterised mutants of tubulin and FtsZ that block GTPase-dependent filament disassembly, forming hyper-stable filaments that severely disrupt function[17-19]. Expression of the equivalent mutant of *H. volcanii ftsZ1* (D250A, Fig 1b) resulted in a very heterogeneous cell-size distribution, including many extensively overgrown cells—the hallmark of a major cell division defect (Fig. 2c, d). Conversely, no division defect was detected during *cetZ1*.E218A expression in *H. volcanii ΔcetZ1* (Fig. 2c), despite the strong dominant-inhibitory behaviour of this mutant in other functions described below. Therefore, CetZ1 is not required for cell division, whereas FtsZ1 plays an important role.

Motility assays revealed a swimming defect in *H. volcanii ΔcetZ1*; no substantial migration in soft-agar medium was observed after 5 days incubation, whereas normal expanding halos of motile cells were observed in strains carrying single deletions of the other five *cetZ* genes (Fig. 2e). Extended incubation showed that *H. volcanii ΔcetZ1* was motile, with a significantly reduced rate compared to wild-type (Fig. 2f). Both strains also showed exclusion zones between adjacent halos (Fig. 2f, Extended Data Fig. 3a, b), indicating repulsive

chemotaxis or sibling colony inhibition[20]. These results suggest that the *ΔcetZ1* mutation primarily affects swimming speed.

To confirm a role for CetZ1 in motility, *cetZ1*.E218A was expressed under control of the tryptophanase gene promoter on the plasmid pTA962[21] in an otherwise wild-type *cetZ* strain (H98). By using increasing tryptophan (Trp) concentrations, chosen to give dose-responsive expression[22], we observed a corresponding reduction in motility compared to the control (Fig. 2g). This dominant-inhibitory effect of *cetZ1*.E218A confirms that CetZ1 has an important role in motility.

In Hv-Ca liquid medium, *H. volcanii* exhibited the irregular-plate (or "disc-shaped"[11]) morphology (Fig. 2d). However, we discovered that cells withdrawn from the leading edge of Hv-Ca soft-agar motile halos were rod-shaped (Fig. 2h, see also Supplementary Video 1). The frequency of rod cells decreased markedly towards the centre of the halo, where very few rods were seen (Extended Data Fig. 3d-f). In contrast, samples from the low-motility *ΔcetZ1* halos were devoid of rods (Fig. 2h). Furthermore, mild expression of *cetZ1*.E218A, which reduced motility compared to wild-type *cetZ1* (Fig. 2g, 0.2 mM Trp), produced much more rounded cells at the leading edge of the halo (Fig. 2h). CetZ1 is therefore essential for the development of a rod-shaped cell type required for efficient swimming.

To determine whether CetZ1 directly controls cell shape changes, wild-type and mutant proteins were overproduced via a plasmid during growth in liquid Hv-Ca. Overproduction of CetZ1 (by 2-3 fold) caused a rod morphology in a substantial fraction of cells compared to the control (Fig. 3a, b). During *cetZ1*.E218A expression, rods were not detected, and the cells instead formed rather jagged, blocky shapes, exhibiting short stalks and other protrusions (Fig. 3a, c). The extent of these phenotypes was sensitive to the level of production (Extended Data Fig. 4). CetZ1 therefore plays a pivotal role in controlling cell shape.

To examine cell shape and protein subcellular localisation, cells producing supplemental FtsZ1 or CetZ1 tagged with the green fluorescent protein (GFP) were visualised. FtsZ1-GFP showed mid-cell bands (rings), which contracted with division furrows, in plates and motile rods (Fig. 4a, b). In plates, CetZ1-GFP was seen throughout the cytoplasm, and localised as spots, short filaments (or patches) of variable intensity at or near the envelope, particularly in regions of relatively high curvature at the cell edges, and at mid-cell and the division furrow (Fig. 4c and Supplementary Video 2). In motile rods, CetZ1-GFP localised at or near one or both poles, as spots, short filaments or end-caps, and at mid-cell in some (Fig. 4d). These

patterns were recapitulated with monomeric-GFP (A206K) and mCherry tags (Extended Data Fig. 5).

Similar to previous FtsZ and tubulin GFP-fusion proteins[23,24], CetZ1-GFP was not fully functional, as its overproduction did not cause rod morphology like untagged CetZ1 (Extended Data Fig. 6a, b). However, overproduced CetZ1-GFP formed dynamic filaments in some cells, typical of the tubulin family (Supplementary Video 3). Furthermore, mild expression of *cetZ1*.E218A-*gfp* inhibited rod formation (Extended Data Fig 6d-f), indicating that the fusion protein interacts with native CetZ1.

Cells producing CetZ1.E218A-GFP showed very low cytoplasmic fluorescence and intense patches of localisation at the cell envelope, predominantly at the regions of high curvature caused by the E218A mutation, such as V-grooves (inward), corners and stalks (Fig. 4e, Extended Data Fig. 6a, g, h, Supplementary Video 4). Consistent with this, electron cryotomography sections of cells producing high levels of untagged CetZ1.E218A showed regions with an additional layer on the inner surface of the envelope (Fig. 4f, Extended Data Fig. 7 and Supplementary Video 5). Time-lapse imaging revealed that CetZ1-GFP localisations were highly dynamic in growing cells, moving on a time-frame of seconds to minutes, whereas the bright CetZ1.E218A-GFP localisations were hyper-stable (Supplementary Videos 6, 7). The synthetic effects of CetZ1.E218A on cell structure, and its corresponding localisation, indicate that it may directly remodel the cell envelope.

Rod development occurred by a transition from a two-dimensional (expansive) growth of plates to a one-dimensional mode in rods, with a concomitant narrowing of cells also clear in some cases; filaments containing CetZ1-GFP were sometimes seen moving along the long axis, particularly at the edges near mid-cell as the rod elongated (Fig. 4g, Supplementary Videos 8-10), suggesting that such filaments represent an active form of CetZ1 in rod development.

Altogether, our results show that CetZ1 is a key part of a dynamic cytoskeleton that reshapes the cell during rod development. The structures and functions of *H. volcanii* CetZ1 and CetZ2, which appears to participate in cell-shape control (Extended Data Fig. 8), together with the appearance of homologs in diverse Euryarchaeota (Fig. 1a and Extended Data Fig. 2), suggest that dynamic regulation of cell shape by FtsZ/tubulin-superfamily proteins may pre-date eukaryotic cells.

The tubulin-like active-site residues and helix 11 in CetZs (Fig. 1) could reflect an early evolutionary divergence of FtsZ and CetZ/tubulin, corresponding to the establishment of a non-cell-division role, followed by a further split of CetZ and tubulin as cell architecture evolved in the Archaea/Eukarya lineage. On the other hand, the slightly higher overall sequence similarities between FtsZ and CetZ would argue that the tubulin-like features of CetZ arose independently of tubulin for similar functional purposes.

The development of rod-shape to attain normal swimming speed indicates that this is an adaptation to optimise swimming, as generally predicted from theoretical considerations of microbial shapes[25-27]. Interconversion of plate and rod cell types would therefore serve as a stop-go switch that responds to the local environment. It is anticipated that *H. volcanii* differentiation and the CetZ family will serve as useful models for cell biology and cytoskeletal evolution.

1 Lowe, J. & Amos, L. A. Evolution of cytomotive filaments: the cytoskeleton from prokaryotes to eukaryotes. *Int J Biochem Cell Biol* **41**, 323-329 (2009).

2 Wickstead, B. & Gull, K. The evolution of the cytoskeleton. *J Cell Biol* **194**, 513-525 (2011).

3 Woese, C. R., Kandler, O. & Wheelis, M. L. Towards a natural system of organisms: proposal for the domains Archaea, Bacteria, and Eucarya. *Proc Natl Acad Sci USA* **87**, 4576-4579 (1990).

4 Baumann, P. & Jackson, S. P. An archaebacterial homologue of the essential eubacterial cell division protein FtsZ. *Proc Natl Acad Sci U S A* **93**, 6726-6730 (1996).

5 Lowe, J. & Amos, L. A. Crystal structure of the bacterial cell-division protein FtsZ. *Nature* **391**, 203-206 (1998).

6 Margolin, W., Wang, R. & Kumar, M. Isolation of an *ftsZ* homolog from the archaebacterium *Halobacterium salinarium*: implications for the evolution of FtsZ and tubulin. *J Bacteriol* **178**, 1320-1327 (1996).

7 Poplawski, A., Gullbrand, B. & Bernander, R. The *ftsZ* gene of *Haloferax mediterranei*: sequence, conserved gene order, and visualization of the FtsZ ring. *Gene* **242**, 357-367 (2000).

8 Wang, X. & Lutkenhaus, J. FtsZ ring: the eubacterial division apparatus conserved in archaebacteria. *Mol Microbiol* **21**, 313-319 (1996).

9 Vaughan, S., Wickstead, B., Gull, K. & Addinall, S. G. Molecular evolution of FtsZ protein sequences encoded within the genomes of archaea, bacteria, and eukaryota. *J Mol Evol* **58**, 19-29 (2004).

10 Oren, A. Molecular ecology of extremely halophilic Archaea and Bacteria. *FEMS Microbiol Ecol* **39**, 1-7 (2002).

11 Burns, D. G. *et al. Haloquadratum walsbyi gen. nov., sp. nov.*, the square haloarchaeon of Walsby, isolated from saltern crystallizers in Australia and Spain. *Int J Syst Evol Microbiol* **57**, 387-392 (2007).

12 Walsby, A. E. Square bacterium. *Nature* **283**, 69-71 (1980).

13 Takashina, T., Hamamoto, T., Otozai, K., Grant, W. D. & Horikoshi, K. *Haloarcula japonica sp. nov*., a new triangular halophilic archaebacterium. *Syst Appl Microbiol* **13**, 177-181 (1990).

14 Mullakhanbhai, M. F. & Larsen, H. *Halobacterium volcanii spec. nov.*, a Dead Sea halobacterium with a moderate salt requirement. *Arch Microbiol* **104**, 207-214 (1975).

15 Marchler-Bauer, A. *et al.* CDD: conserved domains and protein three-dimensional structure. *Nucleic Acids Res* **41**, D348-352 (2013).
16 Yutin, N. & Koonin, E. V. Archaeal origin of tubulin. *Biol Direct* **7**, 10 (2012).
17 Lowe, J., Li, H., Downing, K. H. & Nogales, E. Refined structure of alpha beta-tubulin at 3.5 A resolution. *J Mol Biol* **313**, 1045-1057 (2001).
18 Richards, K. L. *et al.* Structure-function relationships in yeast tubulins. *Mol Biol Cell* **11**, 1887-1903 (2000).
19 Scheffers, D. J., de Wit, J. G., den Blaauwen, T. & Driessen, A. J. GTP hydrolysis of cell division protein FtsZ: evidence that the active site is formed by the association of monomers. *Biochemistry* **41**, 521-529 (2002).
20 Be'er, A., Florin, E. L., Fisher, C. R., Swinney, H. L. & Payne, S. M. Surviving bacterial sibling rivalry: inducible and reversible phenotypic switching in *Paenibacillus dendritiformis*. *MBio* **2**, e00069-00011 (2011).
21 Allers, T., Barak, S., Liddell, S., Wardell, K. & Mevarech, M. Improved strains and plasmid vectors for conditional overexpression of His-tagged proteins in *Haloferax volcanii*. *Appl Environ Microbiol* **76**, 1759-1769 (2010).
22 Large, A. *et al.* Characterization of a tightly controlled promoter of the halophilic archaeon *Haloferax volcanii* and its use in the analysis of the essential *cct1* gene. *Mol Microbiol* **66**, 1092-1106 (2007).
23 Kimble, M., Kuzmiak, C., McGovern, K. N. & de Hostos, E. L. Microtubule organization and the effects of GFP-tubulin expression in *Dictyostelium discoideum*. *Cell Motil Cytoskeleton* **47**, 48-62 (2000).
24 Sun, Q. & Margolin, W. FtsZ dynamics during the division cycle of live *Escherichia coli* cells. *J Bacteriol* **180**, 2050-2056 (1998).
25 Cooper, S. & Denny, M. W. A conjecture on the relationship of bacterial shape to motility in rod-shaped bacteria. *FEMS Microbiol Lett* **148**, 227-231 (1997).
26 Dusenbery, D. B. Fitness landscapes for effects of shape on chemotaxis and other behaviors of bacteria. *J Bacteriol* **180**, 5978-5983 (1998).
27 Young, K. D. The selective value of bacterial shape. *Microbiol Mol Biol Rev* **70**, 660-703 (2006).

Acknowledgements We thank Thorsten Allers for discussion, strains and plasmids, Friedhelm Pfeiffer, Mike Dyall-Smith, Rick Cavicchioli, Ian Charles, Christopher Angstmann and Paul Curmi for discussion, Julie Maupin-Furlow and David Sherratt for plasmids, Michael Johnson and the UTS Microbial Imaging Facility for technical support, Fabrice Gorrec and Sonja Kuhlman for help at the MRC-LMB crystallisation facility, and the European Synchrotron Radiation Facility and Diamond Light Source for service and support. This work was supported by the Medical Research Council, UK (U105184326 to J.L.) and the University of Technology Sydney, Australia. C.B.W. was supported by the NHMRC, Australia (SRF 571905).

Author Contributions Initiated project: I.G.D., K.A.M. and J.L. Designed experiments: I.G.D., C.H.S.A., K.A.M., L.A.A. and J.L. Molecular phylogeny: I.G.D. and E.M.D. Protein

structures: C.H.S.A., J.L., L.A.A and I.G.D. Genetic modification and phenotypes: I.G.D. Light microscopy: I.G.D., J.C.W., L.T., C.B.W. and E.J.H. Image analysis: J.C.W. and I.G.D. Electron cryotomography: Q.W. Wrote the manuscript: I.G.D. Reviewed manuscript: all authors.

Author information Crystal structures have been deposited in the protein data bank (PDB) under the accession codes 4B46 (*H. volcanii* CetZ1), 4B45 (*H. volcanii* CetZ2) and 3ZID (*M. thermophila* CetZ). The authors declare no competing financial interests. Reprints and permissions information is available at www.nature.com/reprints. Correspondence and requests for materials should be addressed to I.G.D. (Iain.Duggin@uts.edu.au).

Methods

Molecular phylogeny Protein sequences were retrieved from the National Centre of Biotechnology Information (NCBI) website. PSI-BLAST[28] was used to identify CetZ sequences using CetZ1 (HVO_2204) from *H. volcanii* as the query sequence. Protein sequences were aligned using MUSCLE[29], and then a phylogenetic tree was generated using Fasttree[30].

Protein purification The open reading frames for *H. volcanii* CetZ1 (HVO_2204) and CetZ2 (HVO_0745) were first amplified from genomic DNA and then cloned into the expression plasmid pHis17[31]. pHis17-HvCetZ1 encoded the complete sequence of *H. volcanii* CetZ1 without additional residues, whereas pHis17-HvCetZ2 encoded the complete sequence of *H. volcanii* CetZ2, adding six histidine residues at the C-terminus. The gene encoding *M. thermophila* CetZ (Mthe_0239, Uniprot A0B5R2) was synthesised codon-optimised (Genscript), and cloned into pET28a (pET28a-MtCetZ), including an additional six histidine residues at the C-terminus.

Escherichia coli C41 strains harbouring the expression vectors were grown in 12 L 2xYT broth supplemented with 100 μg/mL ampicillin or 50 μg/mL kanamycin and grown at 37 °C. Isopropyl-β-D-1-thiogalactopyranoside was added to a final concentration of 1 mM (at A_{600}=1.0), and incubation continued for 18 h at 20 °C. Harvested cells were resuspended in 20 ml per 1itre of bacterial culture of 100 mM Na-HEPES pH 7.0, and then lysed using a cell disruption system (Constant Systems) running at 25 kPSI at 4 °C. The mixture was centrifuged at 45,000 g for 30 min at 4 °C. *H. volcanii* CetZ2 and *M. thermophila* CetZ were purified from the supernatant by immobilized metal affinity chromatography (IMAC), using a 5 ml HisTrap HP column (GE Healthcare) running in 100 mM Tris-Cl (pH 8.5), 500 mM KCl, 0-1 M imidazole gradient), followed by ion exchange with a HiTrap Q column HP (GE Healthcare) running in 25 mM Tris-Cl pH 8.5, with a 0-500 mM KCl gradient. Size-exclusion chromatography was then carried out using a HiLoad Sephacryl S200 16/60 column (GE Healthcare), running in 25 mM Tris-Cl pH 8.5, 200 mM KCl, 1 mM EDTA, 1 mM NaN_3. High yielding fractions were pooled and concentrated to 25 mg/mL before and after size exclusion chromatography in 20 ml capacity, 30 kDa cut-off centrifugal concentrators (Vivaspin). Untagged *H. volcanii* CetZ1 was prepared with the same method, except without the IMAC step.

Crystallisation Initial conditions were identified using the high-throughput MRC-LMB crystallisation facility[32]. All CetZ crystals were produced in 1 µl protein drops containing 50 % protein and 50 % (v/v) precipitant solutions. *H. volcanii* CetZ1 was crystallised in 20 % (w/v) polyethylene glycol Mr 6000, 1 M LiCl, 100 mM Na citrate (pH 4.0). *H. volcanii* CetZ2 was crystallised in 3-3.5 M ammonium sulphate, 100 mM Na citrate (pH 5.0). *M. thermophila* CetZ crystallised in 30 % (v/v) 1,2-propanediol, 20 % (v/v) polyethylene glycol (Mr 400), 0.1 M Na-HEPES (pH 7.5). Artificial mother liquor supplemented to 25 % (v/v) glycerol was used as a cryo-protectant for all proteins during X-ray diffraction image acquisition.

Crystallographic data collection and structure determination Diffraction images were collected from single frozen crystals at European Synchrotron Research Facility beamline ID23eh1 (*H. volcanii* CetZ1 and *M. thermophila* CetZ) or Diamond beamline I03 (*H. volcanii* CetZ2) at 100 K. The wavelengths used for data collection were 0.9 Å and 0.9795 Å at the respective beamlines. Diffraction images were processed with *XDS*[33], *POINTLESS*[34] and *SCALA*[35] software. Initial phases were determined by molecular replacement using *PHASER*[36]. Models were built manually using *MAIN*[37] and refined using *REFMAC*[38] and *PHENIX.REFINE*[39]. Their respective Ramachandran plots were used to validate the structures. The atomic model for *H. volcanii* CetZ1 placed 99.7 % of residues in the most favoured (98 %) region; *H. volcanii* CetZ2 had 98.2 %, and *M. thermophila* CetZ had 99.1 %. No residues from any of the three structures had angles lying in the disallowed (0.2 %) regions. The density connecting the helical C-terminal residues of CetZ2 to the main body of the protein was weak and could not be threaded; therefore, the ordered position of a disconnected C-terminus from the adjacent subunit was deposited as a separate chain (chain B). Crystallographic data are given in Extended Data Table 1.

***H. volcanii* media and culture conditions** Most cultures were grown with Hv-Ca medium[40] modified to contain an expanded trace-elements solution that improved growth and cell shape uniformity. The trace-elements stock solution contained, per litre: 5 g ethylenediaminetetraacetic acid (EDTA), 0.8 g $FeCl_3$, 0.05 g $ZnCl_2$, 0.01 g $CuCl_2$, 0.01 g $CoCl_2$, 0.01 g H_3BO_3, 1.6 g $MnCl_2$, 0.01 g Ni_2SO_4, and 0.01 g H_2MoO_4. The solution was adjusted to pH 7.0 with NaOH, filter sterilised and stored at room temperature. It was diluted 100-fold in media to obtain the working concentration. Where necessary, media was supplemented with auxotrophic requirements[40], or the indicated concentration of L-tryptophan (Trp; Sigma). Hv-YPC medium[40] was used in some experiments, where indicated,

and in genetic modification procedures. For most experiments, cultures were incubated at 45 °C with rotary shaking (150 rpm), and were maintained in log growth (A_{600}<0.8) for at least 2 days prior to sampling (at A_{600}=0.2-0.8), unless otherwise indicated. In addition to preliminary experiments carried out for this study, representative data displayed are representative of at least two biological replicate experiments.

Strain and plasmid construction Strain and plasmid construction information and relevant oligonucleotide sequences are given in Extended Data Table 2. Plasmids for controlled expression in *H. volcanii*, containing the *tna* promoter (*Ptna*)[22], were based on pTA962[21]. The ORF encoding the smRS-GFP variant was amplified from pJAM1020[41], using overlap extension PCR to remove the internal NdeI site, and cloned between BamHI and NotI of pTA962, creating the vector pIDJL40 (see Extended Data Table 2). The *ftsZ1.D250A* and various *cetZ* ORFs were PCR amplified from *H. volcanii* DS70[42,43] DNA, and then cloned between NdeI and BamHI in both pTA962 and pIDJL40. An mCherry ORF was cloned between BamHI and NotI in pIDJL40-*cetZ1*, replacing the *gfp*, to create pIDJL117 (Extended Data Table 2). Point mutations were generated by overlap-extension PCR and fragments were cloned as above, incorporating the following codon substitutions: *ftsZ1*.D250A (GAC>GCC), *cetZ1*.E218A (GAG>GCG) and *gfp*.A206K (GCC>AAG). All PCR-generated fragments were sequence-verified after cloning.

Plasmids for making deletions in *H. volcanii* were constructed by cloning upstream and downstream DNA fragments that flanked each deletion into pTA131[40]. Two stages were used to generate each *cetZ*-deletion plasmid. In the first stage, the upstream DNA fragment amplified from DS70 (primer pairs US-f/US-r, Extended Data Table 2) was spliced by overlap-extension PCR to the corresponding *Ptna-cetZ* fragment that had been amplified with primer PtnaUS-f (CTGGCGAAAGGGGGATGTGCTGC), the *cetZ* ORF reverse primer, and the expression-plasmid template (Extended Data Table 2). The spliced product, in which the native *cetZ* promoter was swapped for *Ptna*, was cloned between the HindIII-BamHI sites of pTA131. These plasmids were demethylated by passage through *E. coli* C2925 (New England Biolabs), and then used in the "pop-in pop-out" method[40], to replace the chromosomal *cetZ* promoters with *Ptna*. Transformants were selected as previously described[40], and then chromosome structures were verified by allele-specific PCR. Preliminary experiments using the resulting strains showed no significant growth defects upon depletion of *cetZ* gene expression by withdrawal of Trp during mid-log growth. In the

second stage, the BglII-BamHI (*Ptna-cetZ*) fragment in each plasmid was replaced with a downstream fragment (amplified with primers DS-f/DS-r, Extended Data Table 2), to create plasmids for deletion of each *cetZ* ORF, as described above. The resulting strains are listed in Extended Data Table 2.

Western blotting CetZ1 rabbit antisera were generated with a synthetic peptide antigen derived from the sequence of the C-terminal region of CetZ1: [C]-QDNIEEIRQESDSNLETLIN-amide (Cambridge Research Biochemicals, UK). Antisera were assayed and verified for specificity (Fig. 2a). *H. volcanii* cells were resuspended in SDS-PAGE sample buffer and then heated (95 °C, 5 min) before analysis by SDS-PAGE and Western blotting (10^{-3} primary antisera dilution) using a Criterion™ electrophoresis system (Bio-Rad) with nitrocellulose membrane (Protran, Whatman) and Chemiluminescence detection (Thermo Scientific) according to standard protocols.

Coulter counting Culture samples were diluted (10^{-2} or 10^{-3}) with 18 % BSW (which included calcium)[40], and then ~10^5 cells were analysed with a Multisizer 4 Coulter Counter (Beckman-Coulter) in the volumetric mode (100 µl), with a 20 µm aperture tube and 18 % BSW as the electrolyte. A 2 µm bead standard (Beckman-Coulter), diluted in 18 % BSW, was used for prior calibration.

Motility assays 1 µL of a mid-log culture in Hv-Ca was inoculated into the subsurface of an Hv-Ca + 0.3 % (w/v) agar plate (20 mL of media per plate), with up to four inoculations per plate from the same liquid culture. Equal cell densities of the inoculum were used for comparison of multiple strains. Plates were incubated with minimal disturbance in a closed plastic bag at 45 °C for 5 days[44], unless otherwise indicated, and then images of the plates were acquired using a densitometer/scanner.

Light Microscopy For most microscopy, a 1 µl sample of culture was placed directly onto a slide prepared with a ~170 µm thick, 1 % agarose pad containing 18 % BSW. A #1.5 coverslip was then placed on top. Phase-contrast and GFP epifluorescence images were then acquired with a Zeiss AxioPlan 2 system with a 1.4 NA phase-contrast objective (Carl Zeiss, Germany).

Time-lapse imaging was performed at 37 °C, with a Nikon Ti with the Perfect Focus™ system and EMCCD camera (Cascade 1K, Photometrics), or the OMX superresolution system with wide-field deconvolution, described further below. Samples were prepared by

placing a 0.5-1 µl sample of growing culture at the centre of a ~0.5 mm thick gel pad (containing media semi-solidified with 0.2-0.3 % agarose or agar) prepared on a coverslip (circular 8 mm diameter, #1.5); this was then inverted onto the base of a 35 mm #1.5 FluoroDish™ (World Precision Instruments, Inc), and then 3 mL of liquid media was added to cover the pad assembly. The lid was replaced and the dish was then incubated on the microscope stage (at 37 °C) for 30 min prior to imaging.

Superresolution imaging was performed with a V3 DeltaVision OMX 3D-SIM Blaze™ system (Applied Precision Inc, a GE Healthcare Company, Issaquah, USA). A solid-state 488 nm laser provided wide-field illumination and images were captured using a 60x 1.4 NA UPlanSApo oil objective (Olympus, Japan), a standard 488 nm excitation and 500-550 nm emission filter set and a scientific CMOS 512 x 512 pixel 15-bit camera (pco.edge, PCO AG, Kelheim, Germany). For wide-field deconvolution imaging, samples were sectioned using a 250 nm step-size and deconvolved using SoftWorX (Applied Precision, GE). For three-dimensional structured illumination (3D-SIM), interference patterns were generated by interfering light beams[45] and samples were sectioned using a 125 nm Z-step size. Raw 3-phase images were then reconstructed as previously described[46,47]. Deconvolved or reconstructed images stacks were 3D rendered and presented using *IMARIS* software (v7.6.4, Bitplane Scientific). Video was prepared using ImageJ[48].

Automated image analysis Phase-contrast and GFP epifluorescence images were analysed using *Mathematica* software (Wolfram Research). Phase-contrast images were first binarised by using a bottom-hat transform with a 30-pixel disk matrix for the kernel. Individual objects (cells) were then identified by using the *Morphological Components* function. Background objects were excluded by three sanity checks using the *Component Measurements* function: (1) The minimum cell size was 200 pixels (1 pixel = 60 nm) with a bounding disk radius of 4 pixels; (2) Fragmented objects were excluded if the ratio of areas calculated by the pixel count and the *Area measurement* parameter lay outside 0.95-1.05; (3) Cells had to contain no holes. The circularity of each cell was calculated as the bounding disk coverage, *i.e.* the percentage area occupied by a cell within the minimal circle that completely contains the cell outline, by using the *Component Measurements* function. To measure cell curvature, a curve was parametrically fitted to the outline of each cell by two Fourier expansions up to the 10th order mode; the relative standard deviation (RSD) of curvature was calculated from this line.

To measure fluorescence association with the cell envelope, epifluorescence images were overlaid with cell outlines from each corresponding phase-contrast image. Fluorescence was then integrated along the normal of the parametric fit of the outline for 3 pixels towards the centre of the cell (Extended Data Fig. 7). In cells displaying localisation of fluorescence (RSD >0.5), the mean fluorescence in areas of high curvature (>2 standard deviations above the mean) was compared to the mean fluorescence intensity of the full perimeter and to the mean of the whole cell. The mean percentage difference between each set of two values across all cells was calculated.

Electron Cryotomography *H. volcanii* were grown in Hv-YPC medium + 4 mM Trp. Mid-log cells were concentrated 10-20 fold by centrifugation and resuspension, mixed with 10 nm protein-A coated colloidal gold particles (Sigma), and then plunge-frozen on Quantifoil R3.5/1 holey carbon-coated TEM grids using a Vitrobot (FEI Company, USA). The grids were then stored under liquid nitrogen. Imaging was performed at 300 kV on an FEI Tecnai G2 Polara transmission electron microscope equipped with a Gatan energy filter (zero-loss peak mode and 20 eV slit width) and a post-GIF 4 x 4 k Gatan Ultrascan camera binned to 2 x 2 k (Gatan, USA). Tilt series were collected around a single axis at 1.5° increment between ± 42° at a pixel size of 0.58 nm or 0.7 nm (at the specimen level) using SerialEM software[49]. The defocus was set at -12 μm and the cumulative dose was < 80 e/Å^2. Tomographic reconstructions were calculated using the *IMOD* tomography package[50].

28 Altschul, S. F. *et al.* Gapped BLAST and PSI-BLAST: a new generation of protein database search programs. *Nucleic Acids Res* **25**, 3389-3402 (1997).

29 Edgar, R. C. MUSCLE: multiple sequence alignment with high accuracy and high throughput. *Nucleic Acids Res* **32**, 1792-1797 (2004).

30 Price, M. N., Dehal, P. S. & Arkin, A. P. FastTree 2--approximately maximum-likelihood trees for large alignments. *PLoS One* **5**, e9490 (2010).

31 Miroux, B. & Walker, J. E. Over-production of proteins in *Escherichia coli*: mutant hosts that allow synthesis of some membrane proteins and globular proteins at high levels. *J Mol Biol* **260**, 289-298 (1996).

32 Stock, D., Perisic, O. & Lowe, J. Robotic nanolitre protein crystallisation at the MRC Laboratory of Molecular Biology. *Prog Biophys Mol Biol* **88**, 311-327 (2005).

33 Kabsch, W. Xds. *Acta Crystallogr D Biol Crystallogr* **66**, 125-132 (2010).

34 Evans, P. Scaling and assessment of data quality. *Acta Crystallogr D Biol Crystallogr* **62**, 72-82 (2006).

35 CCP4. The CCP4 suite: programs for protein crystallography. *Acta Crystallogr D Biol Crystallogr* **50**, 760-763 (1994).

36 McCoy, A. J. *et al.* Phaser crystallographic software. *J Appl Crystallogr* **40**, 658-674 (2007).

37 Turk, D. MAIN software for density averaging, model building, structure refinement and validation. *Acta Crystallogr D Biol Crystallogr* **69**, 1342-1357 (2013).
38 Murshudov, G. N., Vagin, A. A. & Dodson, E. J. Refinement of macromolecular structures by the maximum-likelihood method. *Acta Crystallogr D Biol Crystallogr* **53**, 240-255 (1997).
39 Adams, P. D. *et al.* PHENIX: a comprehensive Python-based system for macromolecular structure solution. *Acta Crystallogr D Biol Crystallogr* **66**, 213-221 (2010).
40 Allers, T., Ngo, H. P., Mevarech, M. & Lloyd, R. G. Development of additional selectable markers for the halophilic archaeon *Haloferax volcanii* based on the *leuB* and *trpA* genes. *Appl Environ Microbiol* **70**, 943-953 (2004).
41 Reuter, C. J. & Maupin-Furlow, J. A. Analysis of proteasome-dependent proteolysis in *Haloferax volcanii* cells, using short-lived green fluorescent proteins. *Appl Environ Microbiol* **70**, 7530-7538 (2004).
42 Hartman, A. L. *et al.* The complete genome sequence of *Haloferax volcanii* DS2, a model archaeon. *PLoS One* **5**, e9605 (2010).
43 Wendoloski, D., Ferrer, C. & Dyall-Smith, M. L. A new simvastatin (mevinolin)-resistance marker from *Haloarcula hispanica* and a new *Haloferax volcanii* strain cured of plasmid pHV2. *Microbiology* **147**, 959-964 (2001).
44 Tripepi, M., Imam, S. & Pohlschroder, M. *Haloferax volcanii* flagella are required for motility but are not involved in PibD-dependent surface adhesion. *J Bacteriol* **192**, 3093-3102 (2010).
45 Strauss, M. P. *et al.* 3D-SIM super resolution microscopy reveals a bead-like arrangement for FtsZ and the division machinery: implications for triggering cytokinesis. *PLoS Biol* **10**, e1001389 (2012).
46 Gustafsson, M. G. L. *et al.* Three-dimensional resolution doubling in wide-field fluorescence microscopy by structured illumination. *Biophys J* **94**, 4957-4970 (2008).
47 Schermelleh, L. *et al.* Subdiffraction multicolor imaging of the nuclear periphery with 3D structured illumination microscopy. *Science* **320**, 1332-1336 (2008).
48 Schneider, C. A., Rasband, W. S. & Eliceiri, K. W. NIH Image to ImageJ: 25 years of image analysis. *Nat Methods* **9**, 671-675 (2012).
49 Mastronarde, D. N. Automated electron microscope tomography using robust prediction of specimen movements. *J Struct Biol* **152**, 36-51 (2005).
50 Kremer, J. R., Mastronarde, D. N. & McIntosh, J. R. Computer visualization of three-dimensional image data using IMOD. *J Struct Biol* **116**, 71-76 (1996).
51 Landgraf, D., Okumus, B., Chien, P., Baker, T. A. & Paulsson, J. Segregation of molecules at cell division reveals native protein localization. *Nat Methods* **9**, 480-482 (2012).
52 Zacharias, D. A., Violin, J. D., Newton, A. C. & Tsien, R. Y. Partitioning of lipid-modified monomeric GFPs into membrane microdomains of live cells. *Science* **296**, 913-916 (2002).
53 Shaner, N. C. *et al.* Improved monomeric red, orange and yellow fluorescent proteins derived from *Discosoma sp.* red fluorescent protein. *Nat Biotechnol* **22**, 1567-1572 (2004).

Figure Legends

Figure 1 | CetZs comprise a distinct tubulin/FtsZ family. (a) Phylogram of the tubulin superfamily across the domains of cellular life. The major taxa containing identified CetZs are shown. Bootstrap support is shown for selected branches. *H. volcanii* CetZ1-6 (Hv1-6) and other CetZ sequences cluster into orthologous groups. Mth CetZ belongs to a non-canonical group that branches from near the centre of the tree. (b) Amino-acid sequence alignments of some conserved regions. Conservation is indicated by red shading (universal), yellow (primarily shared in FtsZ and CetZ), blue (CetZ and tubulin), or green (CetZs). T7 residues mutated to alanine in FtsZ1 (D250) and CetZ1 (E218) are underlined. (c) Structural comparison of FtsZ (PDB 1fsz), *Mth* CetZ, and tubulin (PDB 1jff). (d) *H. volcanii* CetZ2-GTPγS crystal structure shows a straight and untwisted protofilament. The C-terminal α-helix (H11, cyan) superimposes well with the equivalent helix in straight tubulin filaments, although differs from the disordered C-terminus consistently observed in FtsZ. Species abbreviations: Mth – *Methanosaeta thermophila*, Hv – *Haloferax volcanii*, Ca – *Cyanobacterium aponinum*, Ec – *Escherichia coli*, Bs – *Bacillus subtilis*, Mtb – *Mycobacterium tuberculosis*, Hp – *Helicobacter pylori*, At – *Arabidopsis thaliana*, Sc – *Saccharomyces cerevisiae*, Hs – *Homo sapiens*.

Figure 2 | *H. volcanii* CetZ1 is essential for efficient swimming and rod-cell development, but not cell division. (a) Western-blot detection of CetZ1 in mid-log and stationary phase cultures (Hv-YPC medium + 1 mM Trp). Ponceau S pre-staining was used as a loading control (lower panels). CetZ1.E218A (in strain ID59+pTA962-*cetZ1*.E218A) builds-up strongly in non-dividing (stationary phase) cells compared to wild-type CetZ1 (ID59+pTA962-*cetZ1*), which shows net depletion in stationary phase, consistent with the notion that CetZ1.E218A polymer hyper-stability provides increased protection from proteolysis. (b) Cell volume histograms for the six H98.*ΔcetZ* strains during mid-log growth in Hv-Ca medium. (c) Cell volume histograms (log-spaced bins) from cell populations producing CetZ1.E218A (ID59+pTA962-*cetZ1*.E218A, mid-log growth in Hv-Ca + 1 mM Trp), or FtsZ1.D250A (H98+pTA962-*ftsZ1*.D250A, 20 h and 40 h after addition of 1 mM Trp). (d) Phase-contrast images of wild-type (H98+pTA962), *ΔcetZ1* (ID59+pTA962), and FtsZ1.D250A production (H98+pTA962-*ftsZ1*.D250A, 40 h Trp) strains. (e) Motility assays of H98.*ΔcetZ* strains (Hv-Ca + 0.3 % agar, day 5). (f) Time-course motility assays using an alternative genetic background (H53), with four spaced inoculations per plate. The same

results were obtained with the H98 background (not shown). (g) Motility assays (day 5) of wild-type (H98+pTA962), *cetZ1*-expression (H98+pTA962-*cetZ1*) and *cetZ1*.E218A expression (H98+pTA962-*cetZ1*.E218A) strains with the indicated Trp concentrations. High concentrations of Trp partially inhibit growth and motility in all strains. (h) Cells withdrawn from within 2 mm of the halo edge were viewed by phase-contrast microscopy; cell circularity (right) was measured by automated analysis of the images. Leading-edge wild-type cells had a mean width of 0.720±0.013 μm (95 % CI), and SD=0.094 μm, indicating specific regulation of rod-cell width.

Figure 3 | CetZ1 overproduction changes *H. volcanii* cell shape. Mid-log cultures overproducing the indicated proteins (in Hv-Ca + 2 mM Trp) were sampled for phase-contrast microscopy. (a) Images of wild-type vector-only (H98+pTA962), CetZ1 overproduction (H98+pTA962-*cetZ1*) and CetZ1.E218A overproduction (H98+pTA962-*cetZ1*.E218A) strains. (Note: *H. volcanii* cells lie on their larger flat surfaces.) Frequency distributions were obtained for the three strains from automated analysis of cell circularity (b), and relative standard deviation (RSD) of curvature (c). The symbols for data apply to both (b) and (c).

Figure 4 | Subcellular localisation of FtsZ1-GFP and CetZ1-GFP in *H. volcanii*. (a) Fluorescence (green) and phase-contrast (grey) image overlay showing cells producing FtsZ1-GFP (H98+pIDJL40-*ftsZ1*) sampled during mid-log growth in Hv-Ca + 0.2 mM Trp. (b) Cells from a motile halo edge (0.2 mM Trp) showing FtsZ1-GFP, and a cell (inset) showing evidence of division constriction. (c) CetZ1-GFP in mid-log cells (Hv-Ca + 0.2 mM Trp) visualised by regular fluorescence and three-dimensional structured-illumination microscopy (3D-SIM; xy views of 3D-rendered stacks; all 3D-SIM scale bars: 1 μm.) 3D-SIM z-series showed that the localisations are envelope associated (Supplementary Video 2). (d) CetZ1-GFP fluorescence in cells from a motile halo edge (0.2 mM Trp), showing detail of an end-capped cell (inset), and 3D-SIM reconstructions (right) showing single or multiple foci, bi-lobed structures, or short filaments. (e) Phase contrast/fluorescence and 3D-SIM of CetZ1.E218A-GFP during mid-log growth in Hv-Ca + 2 mM Trp. (f) 10 nm sections from electron cryotomography 3D reconstructions, showing detail of the cell envelope in wild-type H98+pTA962) and *cetZ1*.E218A-expressing cells (H98+pTA962-*cetZ1*.E218A), grown in Hv-YPC + 4 mM Trp. Assumed layers of the envelope are indicated, and an extra layer of density on the inner surface of the envelope, which was only clear during CetZ1.E218A overproduction, is indicated by the arrowhead; 3D segmentation analysis showed that the

indicated layer occupies a surface area of 75 nm x 300 nm. (g) Time-lapse imaging of CetZ1-GFP during rod development in Hv-YPC + 0.2 mM Trp (15 min intervals). See also Supplementary Video 8.

Extended Data Figure 1 | CetZ2-GTPγS crystals contain protofilaments and 2D sheets. (a) Expansion of crystal symmetry (PDB 4B45) shows lateral association of tubulin/FtsZ-like protofilaments. The lateral repeat distance of 42.4 Å is slightly shorter than the longitudinal distance (43.2 Å). There is similar packing to the lattice of tubulin dimers in the microtubule wall, although a specific M-loop facilitates the lateral contact in tubulin. CetZ2 shows less intimate contacts between GTPase domains (green) in the protofilament compared to tubulin. (b) 90°-rotated view along the protofilaments. Protofilaments are arranged in the same orientation, creating two different surfaces of the sheet. The H11 helix and C-termini are located on the lower surface as shown (b), and would have the potential to interact with other molecules or surfaces (as seen with the C-terminal tail of FtsZ).

Extended Data Figure 2 | Tubulin-superfamily proteins in Euryarchaeota that contain CetZ. CetZ1 from *H. volcanii* (HVO_2204, Uniprot: D4GVD7) was used in PSI-BLAST searches to identify tubulin-superfamily members in Euryarchaeota. A representative genome from all genera determined to contain a CetZ or non-canonical CetZ was selected (if available), and then all identified superfamily members from these genomes were aligned for generating the phylogram. Bootstrap support is shown for selected branches. The positions of the *H. volcanii* CetZs are indicated (HvCetZ). All species identified to contain a CetZ contained at least one FtsZ; most contained two FtsZs from distinct sub-families. CetZ1 orthologs were identified in all species of Halobacteria analysed, and typically shared ~80 % sequence identity. CetZ2 orthologs were identified in many of these. A number of highly diverse sequences containing recognisable tubulin-superfamily signature motifs (Fig. 1b) were identified in Euryarchaeota, including the classes Thermococci, Methanomicrobia, and Halobacteria (notably, in the rectangular prism-shaped *Haloquadratum walsbyi* – Hwa). These were difficult to robustly classify, however, most were found to branch from near the base of the CetZ-family bough and were referred to as non-canonical CetZs.

Extended Data Figure 3 | The role of CetZ1 in *H. volcanii* motility. Motility assays of the *ΔcetZ1* strain (ID59+pTA962) were performed with closely-spaced (b) or standard-spaced (c) inoculation sites. Exclusion zones were observed between halos after extended incubation (16 days). Irregularities in halo structures were seen in wild-type and mutant halos, which may be

related to colony exclusion (repulsion or inhibition) between local clouds of motile cells. (c) Motility agar plates (containing 0.2 mM Trp), were imaged once daily over 4 days after inoculation. Strains containing wild-type CetZ1 (H98+pTA962 and H98+pTA962-*cetZ1*) show an abrupt development of motile halos from day 3. Strains containing *cetZ1* mutations (H98+pTA962-*cetZ1*.E218A and ID59+pTA962 (*ΔcetZ1*)), were strongly inhibited in motility. (d) A halo of wild-type *H. volcanii* (H98+pTA962) is shown in low and high contrast, showing the high-motility fainter outer zone and the denser population of cells growing more centrally. Samples were withdrawn from the indicated positions (1-4) of the motility halo for microscopy. (e) Cell circularity distributions were then generated from automated computer analysis of images of cells sampled at the four positions (f).

Extended Data Figure 4 | *H. volcanii* cell shape is sensitive to CetZ1 and CetZ1.E218A concentration. (a) Phase-contrast images of wild-type (H98+pTA962), CetZ1-overproduction (H98+pTA962-*cetZ1*) and CetZ1.E218A overproduction (H98+pTA962-*cetZ1*.E218A) strains in mid-log growth in Hv-Ca medium containing the indicated concentrations of Trp. Images of the strains were analysed for cell circularity (b) and the relative standard deviation (RSD) of curvature (c) of cell outlines. The wild-type (WT) control (H98+pTA962, 4 mM Trp) is shown in both (b) and (c). At greater than 2 mM Trp, the circularity and curvature parameters did not increase further. However, during CetZ1.E218A overproduction (4 mM Trp) cells appeared to show slightly larger highly-distorted cells with more noticeable ruffling and protrusions (panel (a), bottom right image). (d) Coulter cell volume analysis of the strains confirmed that CetZ1.E218A overproduction (4 mM Trp) showed slightly larger cells, indicating delayed cell division—a possible effect of significant cell distortion. (e) Western blot analysis of H98+pTA962-*cetZ1* (+CetZ1) and H98+pTA962-*cetZ1*.E218A (+E218A) sampled during mid-log growth in Hv-Ca medium with the indicated concentrations of Trp. Ponceau S pre-staining of the membrane for total protein, as a loading reference, is shown below the CetZ1 Western blot. The levels of CetZ1 increase in response to increasing concentrations of Trp in the medium. CetZ1.E218A showed consistently higher levels compared to wild-type CetZ1, consistent with protofilament hyper-stability resulting in a slower rate of *in vivo* degradation of CetZ1.E218A (see also Fig. 2a).

Extended Data Figure 5 | Localisation of CetZ1-GFP and variants, CetZ1-GFP.A206K and CetZ1-mCherry, in *H. volcanii*. CetZ1 tagged with the GFP variant used primarily in

this study, smRS-GFP[40] was compared to CetZ1 tagged with the A206K mutant of smRS-GFP (which blocks GFP self-association[51,52]) and the mCherry protein[51,53] (which shows red fluorescence in *H. volcanii*). Strains expressing the indicated CetZ1 fusion proteins in pTA962-based plasmids were sampled during mid-log phase growth in Hv-Ca + 0.2 mM Trp (log-phase cells) and from the leading edge of motile halos (0.2 mM Trp).

Extended Data Figure 6 | Expression of *cetZ1-gfp* and *cetZ1*.E218A-*gfp* in *H. volcanii*. (a) Phase-contrast (left) GFP-fluorescence (middle), and Phase/GFP overlay (right) images of strains H98+pIDJL40 (GFP-vector only), H98+pIDJL40-*cetZ1* (+CetZ1-GFP) and H98+pIDJL40-*cetZ1*.E218A (+CetZ1.E218A-GFP) sampled from mid-log growth in strong-overproduction conditions (Hv-Ca + 4 mM Trp). The GFP-vector only fluorescence image is high-contrast, showing low-level background GFP fluorescence, whereas the CetZ1-GFP and CetZ1.E218A-GFP fluorescence images are presented with identical exposure and contrast settings, showing relatively higher background fluorescence for CetZ1-GFP and higher localised fluorescence for CetZ1.E218A-GFP, showing that assembly of the localised protein is stabilised by the E218A mutation (in the GTPase domain of CetZ). (b) Cell circularity distributions for the indicated strains show no stimulation of rod shape during overproduction of either CetZ1-GFP or CetZ1.E218A-GFP. (c) Cell curvature distributions indicate that overproduction of CetZ1.E218A-GFP results in blocky, stalked cells, as seen with untagged CetZ1.E218A (Extended Data Fig. 4). (d) Western blot analysis of CetZ1 in the indicated strains, showing increasing expression of CetZ1-GFP fusion proteins in response to Trp concentration. (e) Motility assays for the indicated strains (H98 background, 0.2 mM Trp), showing significant inhibition of motility by CetZ1.E218A; this may result from higher level production of this protein (see Extended Data Fig. 4e), or stronger inhibition of native CetZ1 function. (f) Cell circularity analysis of cells at the leading edge of the halos in (e) suggests that strong inhibition of rod shape is needed to see an obvious reduction in motility. (Data for wild-type and +CetZ1.E218A strains are reproduced from Fig. 2h.) (g) Cell outlines resulting from the automated cell detection process in phase-contrast and the corresponding GFP-fluorescence images. Magnified images show the normal lines (3-pixels long) on the inside of the cell outline that were integrated to measure fluorescence near the envelope (the closely spaced normal lines give the appearance of a thick outline of the cell). Sections of high curvature (>2 standard deviations above the mean) are shown in green, whereas the remainder is shown in red. (h) A plot of the curvature (red) and the GFP localisation (green) of the magnified cell, measured counter-clockwise from the arrowhead. In automated analysis

of cell populations, the curvature of each whole cell was calculated as the relative standard deviation of this line. Analysis of the strain expressing *cetZ1*.E218A-*gfp* (in Hv-Ca + 2 mM Trp) showed a 73 % greater mean fluorescence in areas of high curvature versus the whole cell, 53 % greater fluorescence for areas of high curvature versus the whole perimeter, and 10 % greater fluorescence for the perimeter versus the whole cell.

Extended Data Figure 7 | Electron cryotomography of *H. volcanii*. Cells growing in Hv-YPC + 4 mM Trp were frozen in vitreous ice to maintain native structure, and then tomographic data were acquired with a 300 kV cryo-TEM. A 10 nm section from the tomographic reconstruction of the whole cell is shown for each. (a) H98+pTA962 ("wild-type") cell, showing cell envelope layers with some structural detail of the outer S-layer visible, a dense granule, particles consistent with ribosomes visible in the outer ~25 % of the cytoplasmic region, and fibres that may be seen underlying the cell envelope. (b) Wild-type (H98+pTA962) cell, with detail of the cell envelope region (inset as per Fig. 4f). (c) Cells overproducing CetZ1.E218A (H98+pTA962-*cetZ1*.E218A), show extensive sections of the envelope with underlying fibres (inset as per Fig. 4f). (Supplementary Video 5 shows a segment image series through a cell, showing the sheet-like structure of the extra layer.) (d) Example showing subtle ruffling of the cell envelope associated with the additional envelope fibres in a cell producing CetZ1.E218A. Scale bars: 100 nm for all panels, and 50 nm for all insets.

Extended Data Figure 8 | Expression of *cetZ2*.E212A affects *H. volcanii* cell shape and motility. The T7-loop mutation *cetZ2*.E212A is equivalent to *cetZ1*.E218A. (a) Expression of *cetZ2*.E212A in motility assays, by addition of increasing concentrations of Trp, inhibits motility, but to a lesser degree than *cetZ1*.E218A. (b) Cells were withdrawn from the leading edge of the indicated motile halos. Mild expression of *cetZ2*.E212A (0.2 mM Trp) partially inhibits rod development, and higher expression (1 mM Trp) strongly inhibits rod formation and produces cells with sharp corners and regions of high curvature, similar to expression of *cetZ1*.E218A (Fig. 4). CetZ2.E218A is therefore dominant-inhibitory to rod development. (c) Coulter cell volumes analysis of cells withdrawn from mid-log cultures of wild-type (H98 + pTA962), *cetZ2*-overexpression (H98 + pTA962-*cetZ2*) and *cetZ2*.E212A-overexpression (H98 + pTA962-*cetZ2*.E212A) strains shows that overexpression of *cetZ2* or *cetZ2*.E212A does not affect cell division. (d) Phase contrast images of cells from the same cultures shown in panel (c). Data obtained from automated analysis of images for each strain is shown in the

plots (d). Unlike *cetZ1* (Fig. 4), overexpression of *cetZ2* in liquid culture did not stimulate rod morphology, indicating that CetZ2 is not a dominant driver of rod formation. However, analysis of cell curvature (lower right panel) showed that expression of *cetZ2*.E212A produced a high-curvature phenotype, similar to *cetZ1*.E218A (Fig. 4), indicating that this mutant specifically interferes with shape regulation in *H. volcanii*.

Extended Data Table 1 Crystallography data collection and refinement statistics.

Footnotes:
*The values recorded in parentheses refer to the highest resolution shell of the dataset collected.
†Diffraction data was truncated at the resolution at which the half-set correlation coefficient fell below 0.7.
‡The values quoted are those calculated and output by PHENIX.REFINE[39] during the final refinement run.
§A set representing 5 % of the reflections collected was randomly selected prior to refinement.
#Mean atomic B-factors for each class of atom described in the final, deposited model.

Extended Data Table 2 *H. volcanii* strains, plasmids and oligonucleotides.

Footnotes:
*Locus identifier (HVO) and Uniprot database (www.uniprot.org) codes are given with the proposed *cetZ* gene names.
†PCR primers shown were used for amplification from DS70 or plasmid DNA as described in the Methods. Relevant restriction enzyme cutting sites are underlined. Complementary primers for generating point mutations were used with the ORF primers in overlap-extension reactions to generate the indicated mutant genes. US/DS-f/r – Upstream/Downstream-forward/reverse. (NS) – no stop codon.
‡smRS-*gfp* was obtained from pJAM1020[41] (from J. Maupin-Furlow). The internal NdeI site was removed by overlap extension PCR to incorporate a silent mutation (CATATG>CACATG), before cloning between BamHI and NotI of pTA962.
§mCherry was obtained from pROD17 (from D. Sherratt). The internal PvuII site was removed by overlap-extension PCR to incorporate a silent mutation (CAGCTG>CAGCTC),

and a mutation in the mCherry template was corrected during pIDJL117 construction (primers not shown).

Fig. 1 Duggin et al.

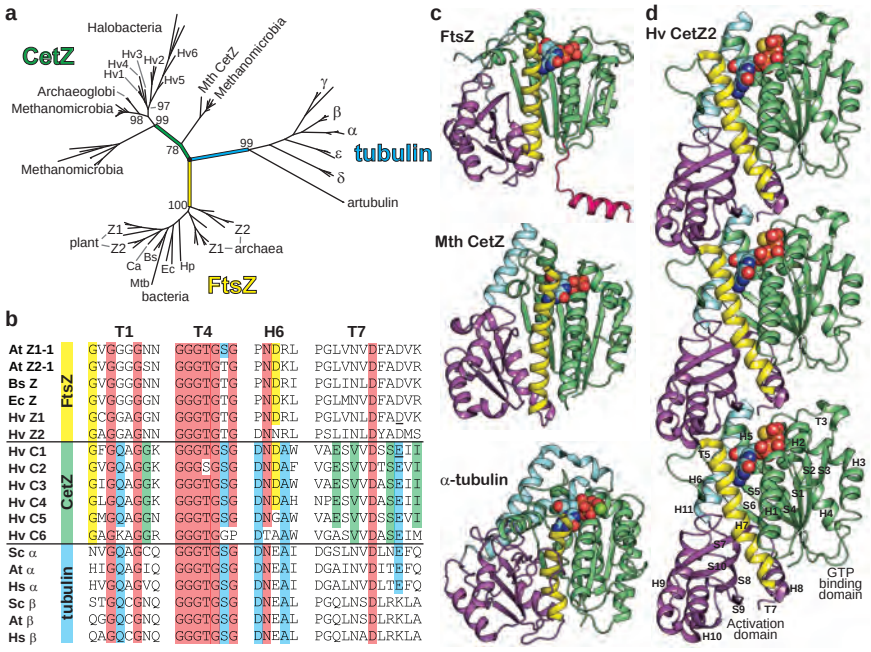

Fig. 2 Duggin et al.

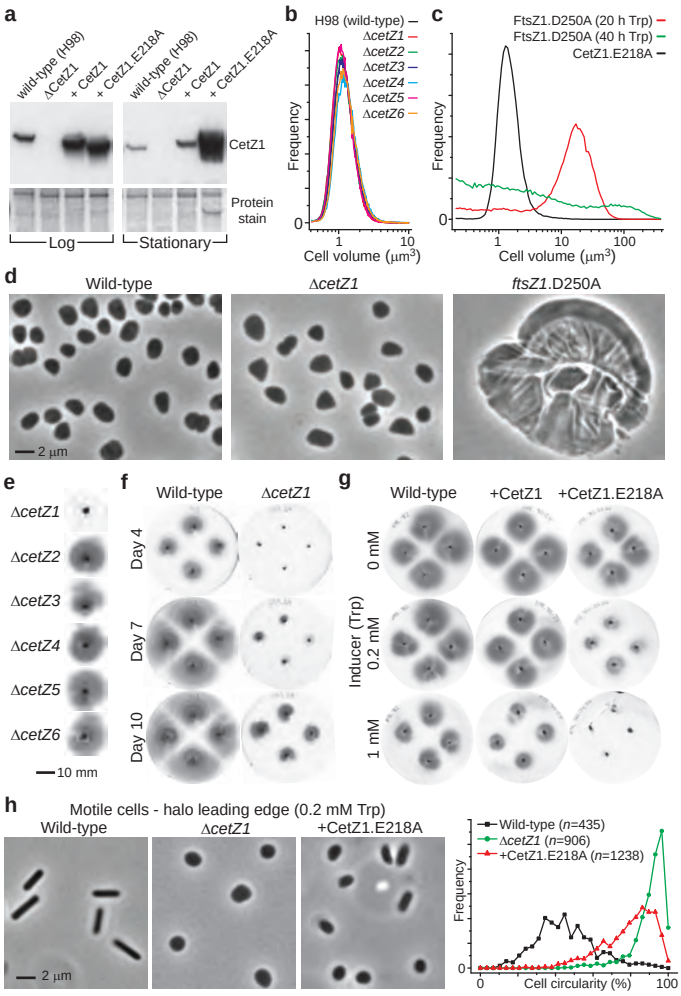

Fig. 3 Duggin et al.

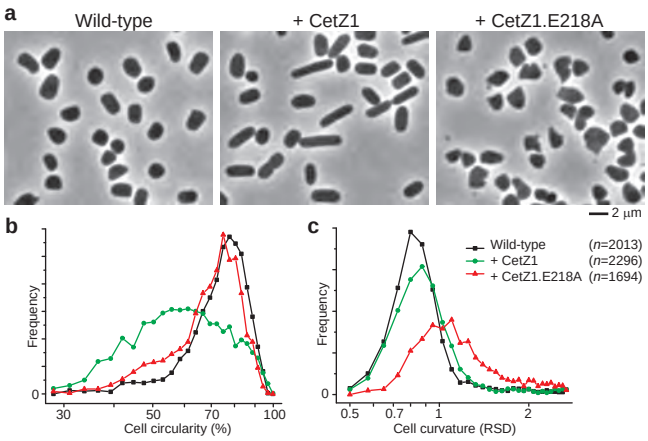

Fig. 4 Duggin et al.

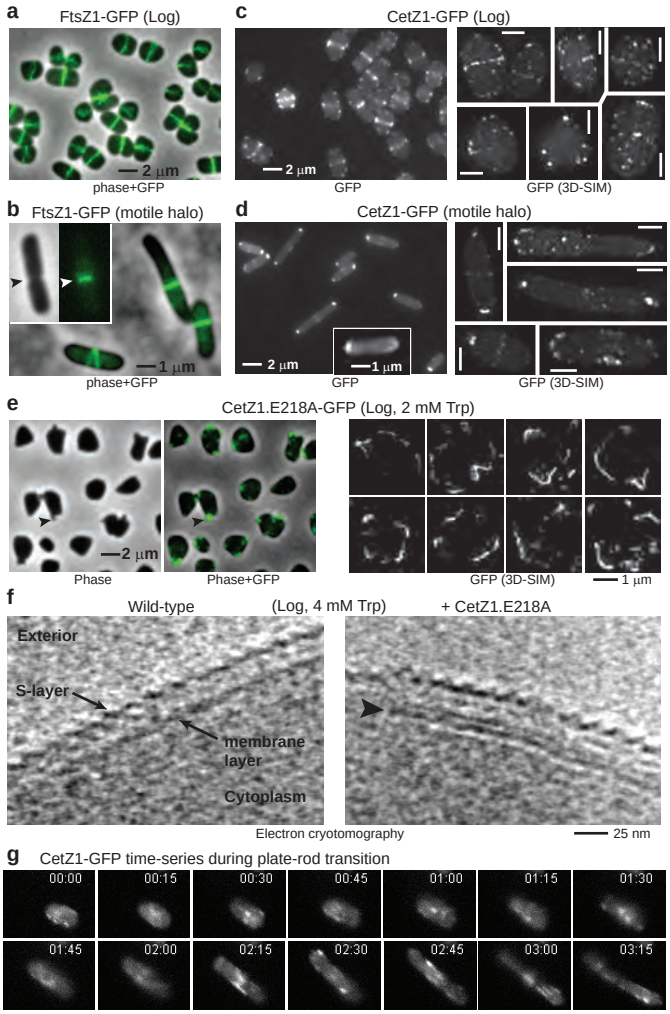

Extended Data Fig. 1 Duggin et al.

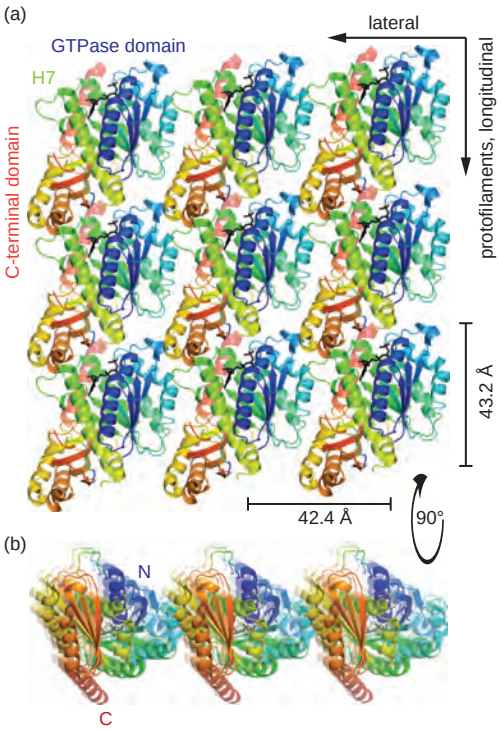

Extended Data Fig. 2 Duggin et al.

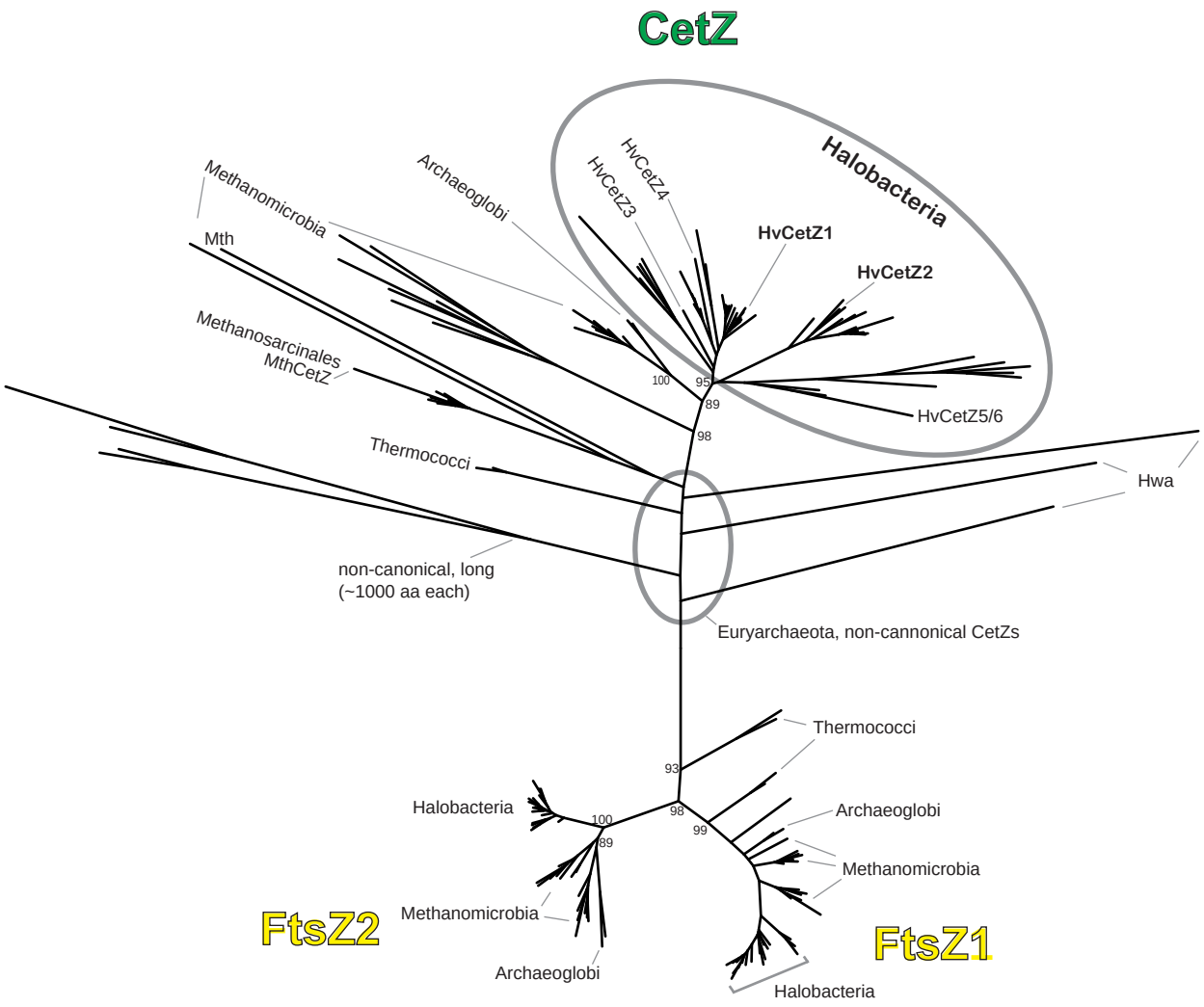

Extended Data Fig. 3 Duggin et al.

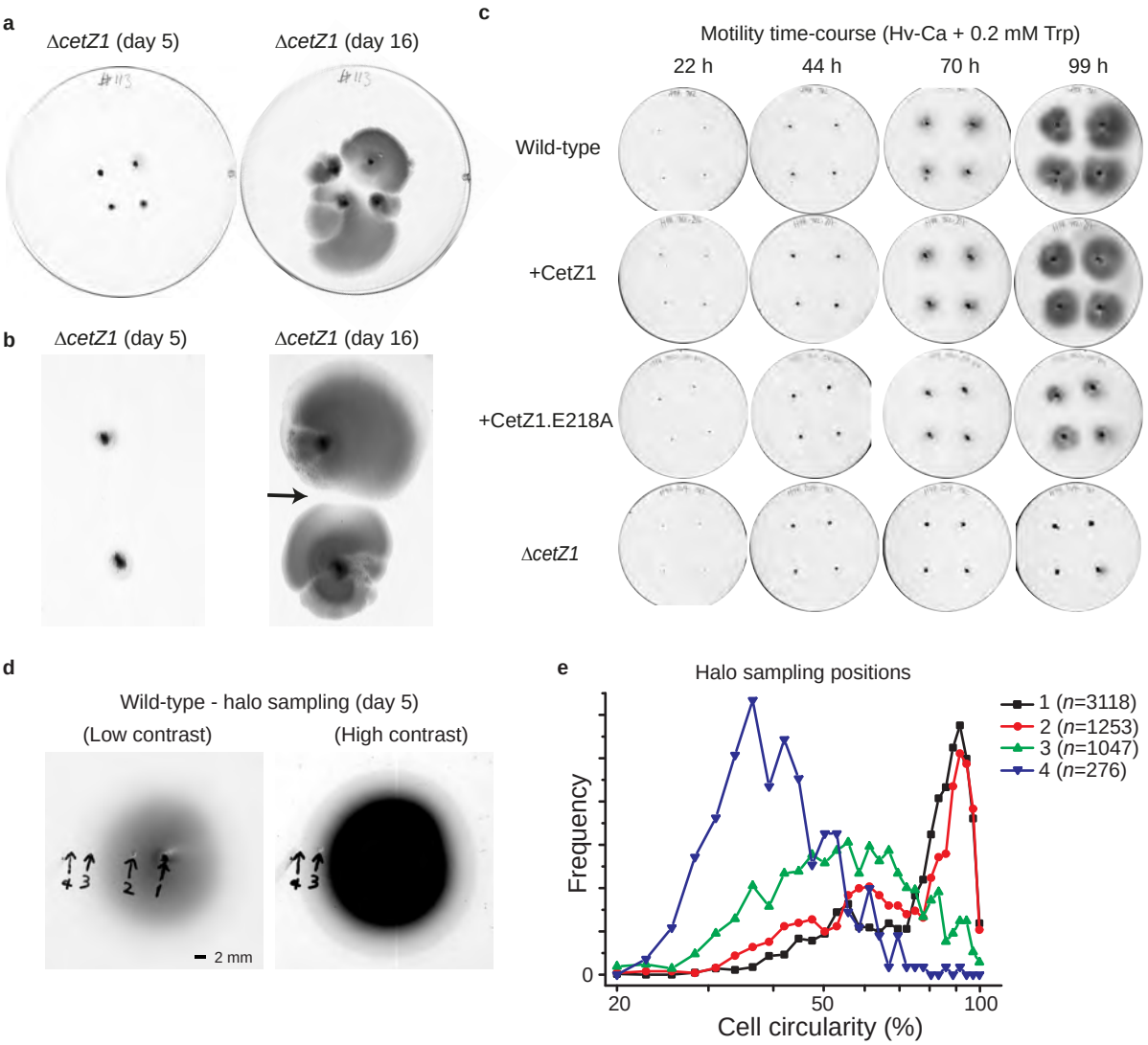

Extended Data Fig. 4 Duggin et al.

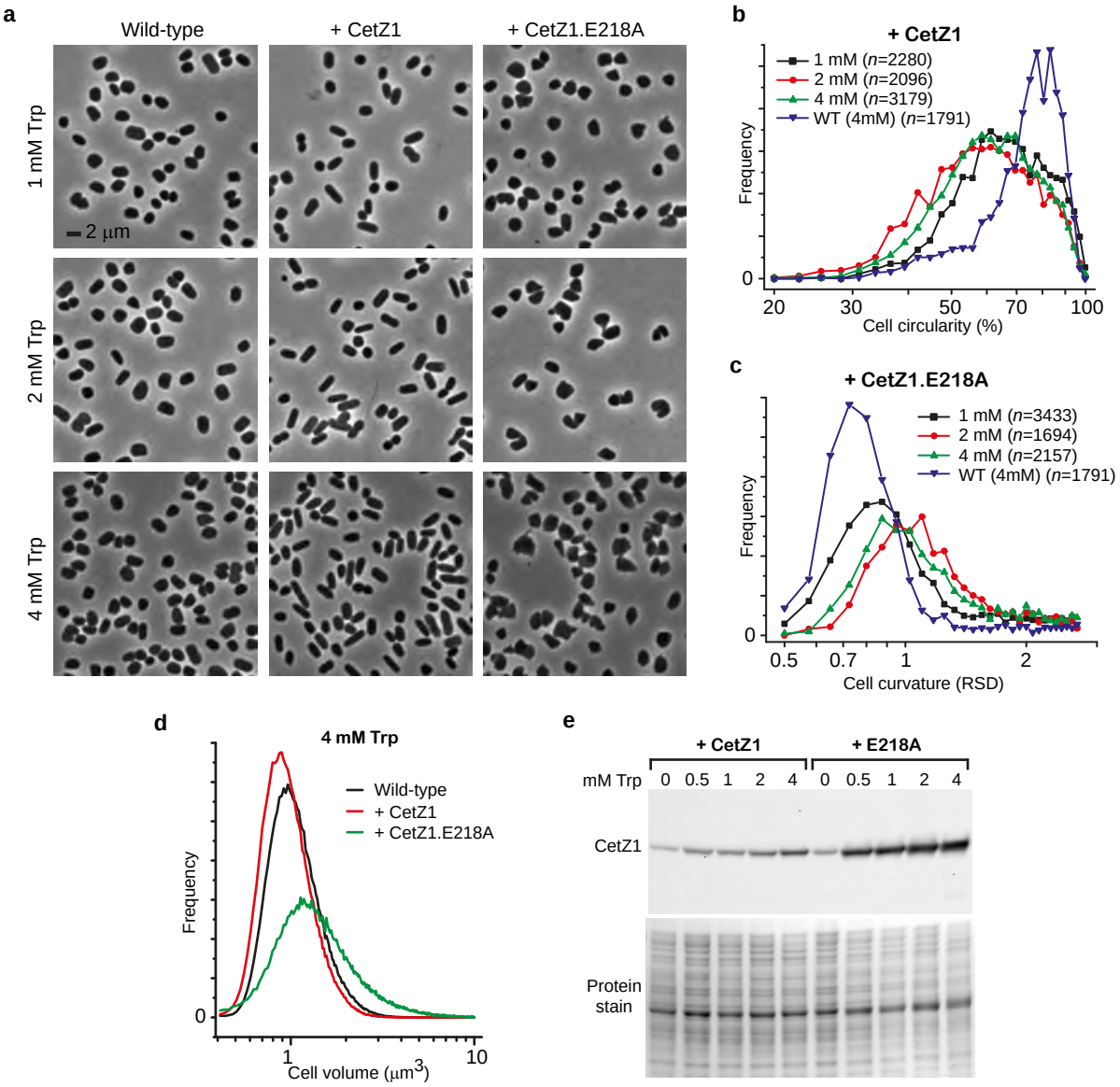

Extended Data Fig. 5 Duggin et al.

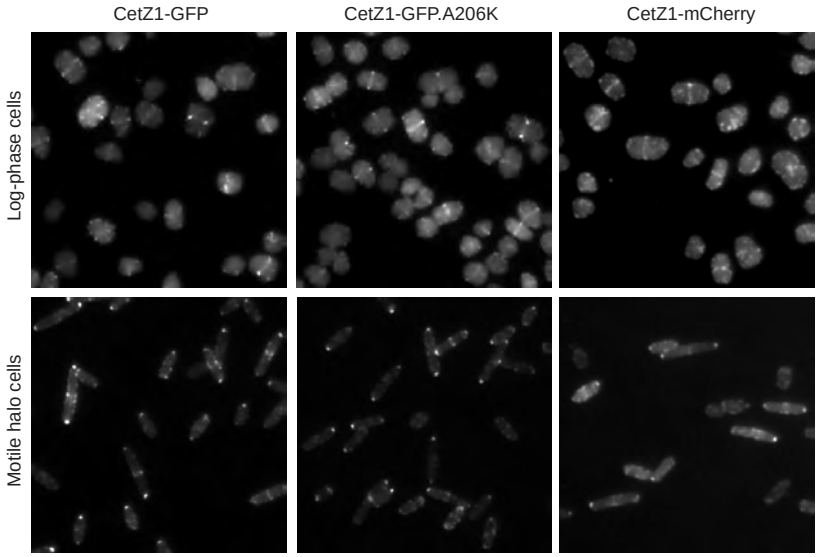

Extended Data Fig. 6 Duggin et al.

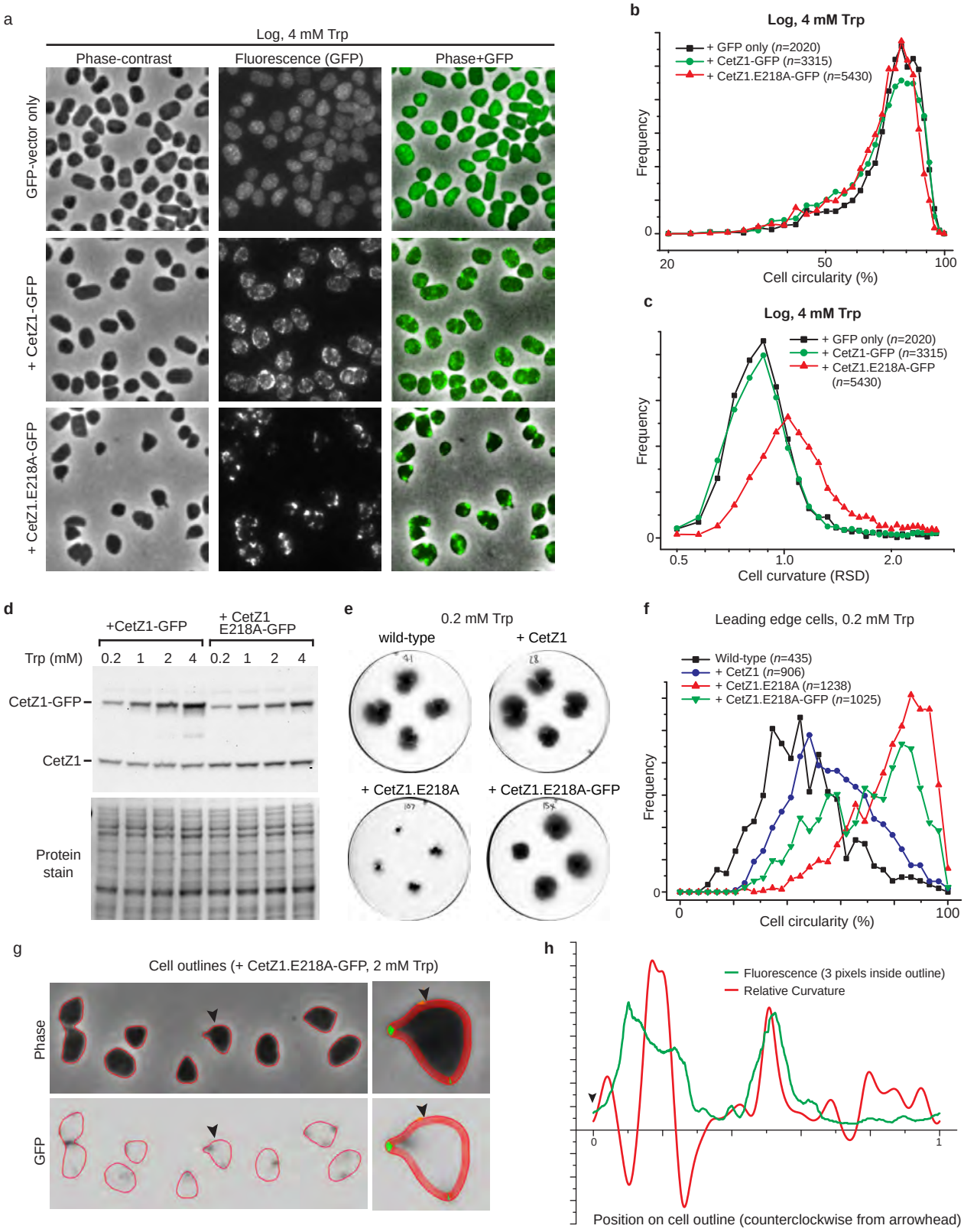

Extended Data Fig. 7 Duggin et al.

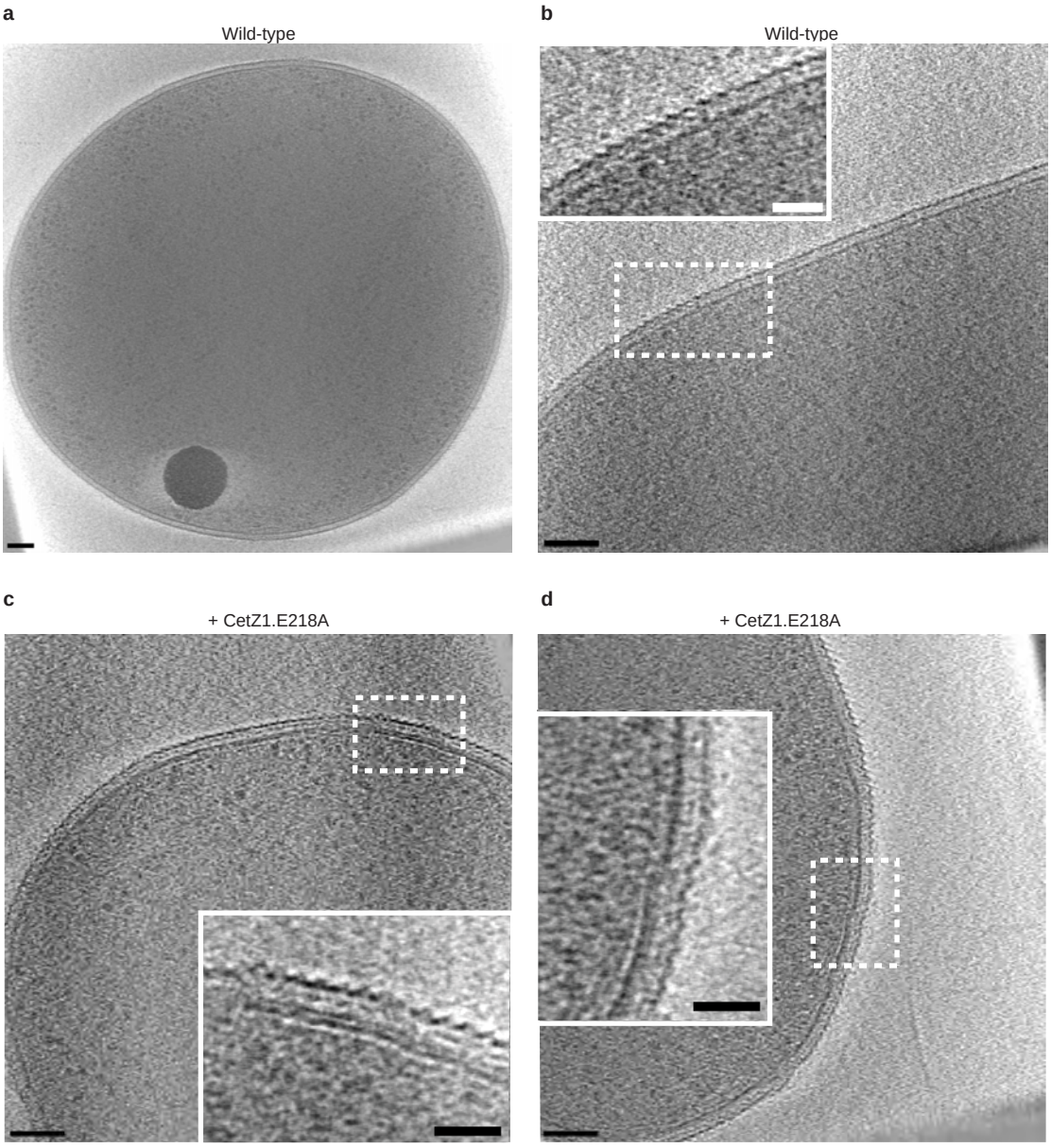

Extended Data Fig. 8 Duggin et al.